International Journal of Heat and Mass Transfer 131 (2019) 863–872

Contents lists available at ScienceDirect

International Journal of Heat and Mass Transfer

journal homepage: www.elsevier.com/locate/ijhmt

Toward high-accuracy and high-applicability of a practical model to predict effective thermal conductivity of particle-reinforced composites

Jeonggeon Kim [a], Yong-Rack Goo [a], Indae Choi [a,b], Songkil Kim [a], Donggeun Lee [a,*]

[a] School of Mechanical Engineering, Pusan National University, Busan 46241, South Korea
[b] Department of Mechanical and Aerospace Engineering, Seoul National University, Seoul 08826, South Korea

ARTICLE INFO

Article history:
Received 23 August 2018
Received in revised form 26 October 2018
Accepted 21 November 2018

Keywords:
Particle-reinforced composites
Effective thermal conductivity
Practical model prediction
Lattice Boltzmann simulations

ABSTRACT

A particle-reinforced composite material is a matrix with thermally conductive particles that has a diverse range of applications from electronics to energy harvesting/storage systems. In the engineering design of a particle-reinforced composite material for application, it is crucial to accurately and practically predict its effective thermal conductivity. Here, we report the development of a simple analytical model for predictions with improved accuracy and applicability. Comprehensive evaluation of existing models was first conducted to clarify their limitations in prediction accuracy and applicability to various experimental conditions. To overcome the challenges of the existing models, our new model was derived to consider the effect of shape, particle aggregation, and mutual interaction of particles on effective thermal conductivity. Lattice Boltzmann simulations were conducted to obtain a quasi-universal coefficient representing interactions of particles, whereas a shape coefficient characterizing microstructures of aggregated particles was obtained from experimental data available from literature. As a result, our model prediction outperformed the existing models in its prediction accuracy, and it could be applicable to any experimental circumstances where previous model predictions are inappropriate to use.

1. Introduction

Particle-reinforced composites, which consist of a matrix with thermally conductive particles, have been widely used in a variety of applications with their engineered thermal conductivities. For example, polymer composites mixed with particles having a higher thermal conductivity have been used in place of metallic components in heat exchangers [1,2] and in fuel cells [3] due to their light weight and enhanced thermal conductivity. Particularly in electronics application, thermally conductive but electrically insulating particles have been added to insulating materials such as polymers. These composites have been used as semiconductor device packaging material or thermal interface material [4,5,16] and more recently as a heat-dissipating component of flexible electronic devices [6].

For this purpose, the particles are normally selected to have a (100–1000 times) higher thermal conductivity than the matrix material. For example, a polymer matrix having a thermal conductivity of 0.17–0.58 W/m K was mixed with inorganic conductive particles such as aluminum nitride with 150–220 W/m K or boron nitride with 29–300 W/m K [7]. Since the heat-conduction performance of such composites has been characterized by their effective thermal conductivity, a priori prediction of the effective thermal conductivity is a prerequisite for the efficient design of such composites.

Since the late 19th century, a large number of analytical models have been proposed to predict effective thermal conductivities for a variety of composite structures. The table in Appendix A summarizes the most popular models with their functional forms. Most of the early models, classified as Group A in the table, describe the effective thermal conductivity (k_{eff}) as a function of volume fraction (v_f) and thermal conductivity (k_p) of particles as well as the thermal conductivity of matrix (k_m). Although the three variables v_f, k_p, and k_m are primary factors in determining k_{eff}, many secondary factors exist, such as shape, orientation, spatial distribution, and aggregation of particles, as well as contact resistance (or Kapitza resistance) in between a particle and matrix [8]. Models that belong to Group B consider the distribution effect of particles, while models in Group C revolve around the morphology of non-spherical particles. One model in Group D was developed to reflect the orientation effect of non-spherical particles, while the factor of contact resistance was not considered in this study (this will be discussed in Section 3).

* Corresponding author.
E-mail address: donglee@pusan.ac.kr (D. Lee).

https://doi.org/10.1016/j.ijheatmasstransfer.2018.11.107
0017-9310/

Despite the relatively large number of previous models, such former models have had limited success in the prediction of k_{eff} with conditioned evaluation of their predictions. To our knowledge, there is no report of comprehensive performance evaluations of the previous models under various conditions. Thus, it is difficult to know what the best model is under a given condition of interest, for example, for enhancing heat dissipation. It is also noted that the abovementioned secondary factors are closely interrelated, particularly when increasing the volume fraction of particles to attain the required level of heat dissipation [8]. At high volume fractions, initially spherical particles have more chance to form an elongated aggregate that can be treated as a non-spherical particle with a large aspect ratio, or mutual influence between particles becomes significant as they get closer to each other. This complexity might explain why these models have large discrepancies in the prediction against experimental data (this will be discussed in Section 2).

More recently, various full numerical simulations have been undertaken to estimate effective thermal conductivities for more practical (complicated and large-scale) composite structures [9–12]. Although these numerical methods are clearly helpful for understanding microstructure-dependent heat conduction characteristics, the methods are not likely to be suitable for more complicated circumstances such as ash deposition in power plants [13] and laser sintering of metallic powders in 3D printing [14,15]. The reason for this is that too large a calculation load is required for the analysis of combined transient heat transfer between the surrounding gas and the microporous composites. Conclusively, a prediction model should be further simplified to reduce computational steps and time along with improved accuracy.

The first objective of this study is therefore to evaluate the previous analytical models with increasing k_p/k_m and v_f of particles, targeting enhanced heat dissipation applications. The results showed that most of the previous models had a similar trend in the predictions of k_{eff} when increasing k_p/k_m, and were reduced to a single asymptotic functional form at the extreme condition ($k_p/k_m \to \infty$). Secondly, based on this asymptotic behavior, a new analytical model was derived to accommodate the secondary factors of shape, aggregation, and mutual interaction of particles in addition to the primary factors, and further simplified by employing two semi-empirical coefficients. A Lattice Boltzmann simulation was also performed to provide reliable data for ideal composites, and its results were used to determine the two coefficients. Moreover, the present new model was applied to experimental data from literature where the internal microstructures of particle-reinforced composites were available with SEM images. As a result, the present model best predicted effective thermal conductivities of three types of particle-reinforced composites among all the previous analytical models considered. Finally, we propose an empirical equation to estimate an aspect ratio of aggregates at a given volume fraction and conductivity ratio, and showed that the present model enabled the prediction of effective thermal conductivity of any particle-reinforced composites with reasonably high accuracy even when their microstructures are unknown.

2. Comprehensive evaluation of previous models and their asymptotic behaviors at extreme conditions

This section is devoted to the comprehensive evaluation of eleven previous models that have frequently been used for the prediction of k_{eff}. Prediction results of the models were compared with experimental data from literature in three distinct ranges of the ratio α defined by k_p/k_m ($1 < \alpha < 100$; $100 \le \alpha < 1000$; $\alpha \ge 1000$). Note that the experimental data we considered here were selected only within literature where k_p and k_m were clearly reported [16–28], and that all of the data correspond to the condition of $1 < \alpha \le 1700$ and $0 \le v_f \le 0.4$.

Table 1 summarizes the prediction accuracy of each model in terms of an average error E defined by Eq. (1) [29,30]:

$$E = \frac{1}{N}\sum_{i=1}^{N}\frac{|k_{exp} - k_{model}|}{k_{exp}} \times 100 \quad (1)$$

where N is the total number of experimental data considered, k_{exp} is an effective thermal conductivity measured by experiment, and k_{model} is the corresponding prediction data. In Table 1, the prediction errors are highlighted by the change in the table cell color from white to dark gray. The white cells indicate that the model prediction error is less than 10%, the pale-gray cells denote 10–20% prediction errors, and the dark-gray cells imply the most inaccurate predictions with $E > 20\%$. By counting the number of dark-gray cells in each column of the table, one may intuitively notice that the prediction errors tend to increase as the ratio α ($\equiv k_p/k_m$) increases from the left to the right column, that is, from $1 < \alpha < 100$ to $100 \le \alpha < 1000$ and $\alpha \ge 1000$.

When the least conductive particles are considered as $1 < \alpha < 100$, Bruggeman's asymmetric model is the most accurate within 3% of error with respect to experimental data. Nine of the eleven models prove to be acceptable in prediction accuracy with $E < 20\%$, whereas the parallel model and the co-continuous model do not work properly, revealing 262% and 74% errors, respectively. When $100 \le \alpha < 1000$, only four of the eleven models can make it within 20% error, and the models entirely experience a significant decrease in the prediction performance. When α increases to over 1000, the performance of the models drastically degrades, leaving behind only three models whose prediction errors are in the range of 20–25%, that is, Cheng–Vachon's model, Lewis–Nielsen's model, and Bruggeman's asymmetric model.

To understand these peculiar but common behaviors of the previous models under high α conditions, we investigated the increasing trends of a dimensionless conductivity of k_{eff}/k_m from the model predictions when increasing k_p/k_m (= α) up to infinity. Based on the results, the eleven models could be discriminated into two groups showing two asymptotic behaviors termed as 'a diverging model' and 'a converging model.' Fig. 1(a) shows the result of a parallel model as representative of the diverging model, where k_{eff}/k_m denotes a very sharp increase without limitation, starting from a slow and gradual increase. In Fig. 1(b), however, the Maxwell–Eucken model shows a certain difference in that k_{eff}/k_m initially increases but levels off and then remains almost constant even when $\alpha \ge 1000$. This type of model corresponds to the converging model. Since no limited increase of thermal conductivity goes against the experimental results, such diverging models including a geometric mean model and a co-continuous model have been ruled out for further consideration. In fact, the three diverging models were the ones denoting unacceptably high prediction errors (76–6036%) when $\alpha \ge 1000$ in Table 1.

Of particular interest is seeing how the converging models behave at the limit of α. Hence, we derived asymptotic functional forms of the models by taking α to infinity in the original formulae in Appendix A and summarizing them in Table 2. As expected, all of the converged models in Table 2 do not depend on α anymore, explaining the level-off limit. Although Bruggeman's symmetric model was classified under the converged models, its asymptotic form indicates that there is a singular point in volume fraction (see Table 2). When the volume fraction v_f approaches 1/3, the term of k_{eff}/k_m diverges irrespective of any other parameters. Thus, this model was also excluded from further consideration.

Table 1
Summary of average errors between existing prediction models and experimental data from literature. This is divided into three ranges of the thermal conductivity ratio. The table cells were shaded from white to dark gray in an attempt to visualize the prediction errors.

Model name	Average error	Model name	Average error	Model name	Average error
$k_p/k_m < 100$		$100 \le k_p/k_m < 1{,}000$		$k_p/k_m \ge 1{,}000$	
Parallel	262%	Parallel	2,072%	Parallel	6,036%
Series	18%	Series	36%	Series	47%
Geometric	8%	Geometric	25%	Geometric	76%
Maxwell–Eucken	5%	Maxwell–Eucken	22%	Maxwell–Eucken	34%
Bruggeman symmetric	11%	Bruggeman symmetric	56%	Bruggeman symmetric	648%
Cheng–Vachon	4%	Cheng–Vachon	13%	Cheng–Vachon	20%
Lewis–Nielsen	6% (sphere)	Lewis–Nielsen	22% (sphere)	Lewis–Nielsen	31% (sphere)
	4% (aggregate)		13% (aggregate)		23% (aggregate)
Zhou (Dispersed)	11%	Zhou (Dispersed)	30%	Zhou (Dispersed)	40%
Bruggeman asymmetric	3%	Bruggeman asymmetric	16%	Bruggeman asymmetric	23%
Russell	10%	Russell	17%	Russell	27%
Co-continuous	74%	Co-continuous	322%	Co-continuous	542%

3. Derivation of a new simplified model

This section describes how to formulate a generalized function so that it includes the effects of the aforementioned primary and secondary factors. The formulation was started from an ideal circumstance where a spherical particle of radius r_p is located in an infinite matrix. Initially given a constant temperature gradient ∇T_0 to the matrix, the temperature field is distorted around the particle, yielding the temperature gradient profile in a spherical coordinate, as seen in Eq. (2) [31]:

$$\nabla T = \nabla T_0 + \left(\frac{r_p}{r}\right)^3 \frac{k_p - k_m}{k_p + 2k_m}[3\hat{n}\hat{n} - I] \cdot \nabla T_0 \equiv \nabla T_0 + K_1\left(\vec{r};\vec{r_1}\right) \cdot \nabla T_0 \quad (2)$$

where K_1 is the operator that reflects the temperature gradient distortion arisen from the single particle, $\vec{r}$ represents the position vector to measure the temperature gradient, and $\hat{n}$ is the radial unit vector.

If N number of spherical particles exist in the matrix, the temperature gradient becomes more complicated due to complex inter-particle interactions, as seen in Eq. (3) [31]:

$$\nabla T = \nabla T_0 + \sum_{i=1}^{N} K_1\left(\vec{r};\vec{r_i}\right) \cdot \nabla T_0 + \sum_{i<j}^{N} K_2\left(\vec{r};\vec{r_i},\vec{r_j}\right) \cdot \nabla T_0 + \sum_{i<j<k}^{N} K_3\left(\vec{r};\vec{r_i},\vec{r_j},\vec{r_k}\right) \cdot \nabla T_0 + \cdots \quad (3)$$

where K_n represents n number of particles' contribution to the temperature gradient distortion, and $\vec{r_i}$ is the position vector of the i-th particles. To date, there have been few reports on K_2, however their proposed functional forms are not consistent and sometimes controversial. Apart from that, there is no analytic form available for K_3 and higher-order terms. For simplicity, in this study, the temperature gradient distortion is first approximated by neglecting K_2 and the higher-order terms in Eq. (3), and introducing an additional constant C_1 to consider those inter-particle interactions instead, as shown in Eq. (4):

$$\nabla T \cong \nabla T_0 + C_1 \sum_{i=1}^{N} K_1\left(\vec{r};\vec{r_i}\right) \cdot \nabla T_0 \quad (4)$$

Here, it is worth noting Maxwell–Eucken's model, in which N number of particles in a matrix were treated as an artificial spherical composite of radius R comprising the particles [32]. According to Maxwell's approximation [33], at sufficiently large radial distances ($r \gg R$), the temperature gradient ∇T can be simplified as the superposition of the result from each particle, such that K_1 in Eq. (4) is simply replaced by its definition in Eq. (2) [31,32]. Hence, Eq. (4) is now rewritten as:

$$\nabla T = \nabla T_0 + C_1 N\left(\frac{r_p}{r}\right)^3 \frac{k_p - k_m}{k_p + 2k_m}[3\hat{n}\hat{n} - I] \cdot \nabla T_0 \quad (5)$$

Again, at the far field, the artificial spherical composite can be seen as a single particle having a thermal conductivity of k_{eff} in

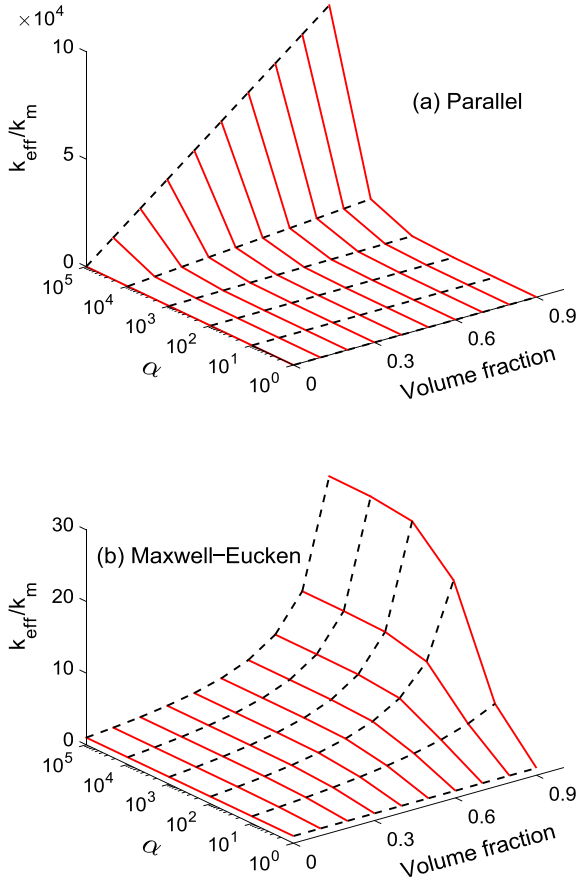

Fig. 1. Variations of k_{eff}/k_m with volume fraction and thermal conductivity ratio (α); (a) Parallel model, which is divergent at high thermal conductivity ratio, (b) Maxwell–Eucken's model, which is convergent at high thermal conductivity ratio.

Table 2
Asymptotic forms of previous models at the extreme condition ($\alpha \to \infty$).

Model name	Asymptotic form	Model name	Asymptotic form
Series	$\frac{k_{eff}}{k_m} \to \frac{1}{1-v_f}$	Zhou	$\frac{1+v_f^{4/3}+v_f^{5/3}}{1-v_f}$
Maxwell–Eucken	$\frac{1+2v_f}{1-v_f}$	Bruggeman asymmetric	$\frac{1}{(1-v_f)^3}$
Bruggeman symmetric	$\frac{1}{1-3v_f}$	Russell	$\frac{1}{1-v_f^{1/3}}$
Cheng–Vachon	$\frac{1}{1-\sqrt{1.5}v_f^{1/2}}$	Hatta–Taya	$\frac{1+\left(\frac{2}{3S_{11}}+\frac{1}{3S_{33}}-1\right)v_f}{1-v_f}$
Lewis–Nielsen	$\frac{1+Av_f}{1-\psi v_f}$	Hamilton–Crosser	$\frac{1+(n-1)v_f}{1-v_f}$

an infinite matrix. Thus, the equation for the single-particle case, that is, Eq. (2) can be extended to the many-particle problem by replacing r_p^3 and k_p with R^3 and k_{eff}, respectively, as:

$$\nabla T = \nabla T_0 + \left(\frac{R}{r}\right)^3 \frac{k_{eff}-k_m}{k_{eff}+2k_m}[3\hat{n}\hat{n}-I]\cdot\nabla T_0 \tag{6}$$

Equating Eqs. (5) and (6), an explicit equation for k_{eff} is readily obtained as:

$$\frac{k_{eff}-k_m}{k_{eff}+2k_m} = C_1\frac{Nr_p^3}{R^3}\frac{k_p-k_m}{k_p+2k_m} \tag{7}$$

Here, recalling that Nr_p^3/R^3 is equal to the volume fraction of particles v_f, Eq. (7) is now rearranged with respect to k_{eff}/k_m as:

$$\frac{k_{eff}}{k_m} = \frac{1+2C_1\beta v_f}{1-C_1\beta v_f} \tag{8}$$

where β represents $(k_p\text{-}k_m)/(k_p+2k_m)$ and goes to unity at high thermal conductivity limits ($\alpha \to \infty$). Under this limiting condition, if the inter-particle interaction is neglected as $C_1 = 1$ in Eq. (8), this equation is readily reduced to the asymptotic function of the Maxwell–Eucken model in Table 2.

Recalling that Maxwell–Eucken's asymptotic function and Eq. (8) are valid only for spherical particles, the numerical value of 2 in Eq. (8) might relate to the spherical shape of particles. In addition, an apparent difference arises from the coefficient of v_f in the denominator per model in Table 2; 2 in the Maxwell–Eucken model for spherical particles vs $(n\text{-}1)$ in the Hamilton–Crosser model or $2/(3S_{11})+1/(3S_{33})\text{-}1$ in the Hatta–Taya model dealing with non-spherical particles. From this finding, the value of 2 in Eq. (8) and in the definition of β is replaced with a shape coefficient C_2 in an attempt to extend Eq. (8) to non-spherical particles as:

$$\frac{k_{eff}}{k_m} = \frac{1+C_2C_1\beta v_f}{1-C_1\beta v_f} \tag{9}$$

where β is now $(k_p\text{-}k_m)/(k_p+C_2k_m)$, and C_2 is defined as a function of aspect ratio (r_a) of ellipsoidal (non-spherical) particles, as shown in Eq. (10) [34].

$$C_2 = \frac{2S_{11}^{-1}+S_{33}^{-1}}{3}-1,\quad S_{11} = \frac{r_a}{2(r_a^2-1)^{\frac{3}{2}}}\left(r_a\sqrt{r_a^2-1}-\cosh^{-1}(r_a)\right), S_{33} = 1-2S_{11} \tag{10}$$

In this way, Eq. (9) was developed to encompass the primary factors and most of the secondary factors such as inter-particle interaction and the non-spherical shape of particles, targeting extreme (high α) conditions. The inter-particle aggregation effect can readily be included in Eq. (9) through the coefficient of C_2, as long as the aggregates' shape or the internal microstructure of the composites is known. (Note also that Eq. (9) was developed to be self-consistent.) For example, when $\alpha \to \infty$ is at a fixed v_f, β becomes independent of k_p (or α), so does k_{eff}/k_m, irrespective of the particles' shape, as observed in Fig. 1(b). As another limiting condition, when $\alpha \to 1$, β becomes zero, and thus Eq. (9) returns $k_{eff} = k_m$.

The only exceptional factor not taken into account in Eq. (9) is the contact (or interfacial) resistance that is also called Kapitza resistance (R_k). The Kapitza resistance is measured by a length scale defined by $r_k = R_k k_m$ [35] and the r_k is called Kapitza radius. The Kapitza resistance creates an adverse effect in a manner that inhibits heat conduction at the particle-matrix interface, so that it strongly depends on how much interfaces are available. As particles become larger at a fixed volume fraction, the Kapitza resistance will play a limited role along with a decrease in total interface area. According to Every et al. [35], a ratio of r_k/r_p can be regarded as a measure of relative significance of Kapitza resistance. For instance, when $r_k/r_p \le 0.1$, the Kapitza resistance is approximately negligible.

Meanwhile, normally micron-sized conductive particles are added in a less-conductive polymer matrix for improving heat dissipation. Given a typical range of interfacial resistance (2–100 $\times$ 10^{-9} m^2K/W) at room temperature [36], the corresponding Kapitza radius was calculated as ranging from 10^{-10} to 10^{-8} m for a typical polymer matrix ($\sim 10^{-1}$ W/m K). Thus, the Kapitza radius is now several orders of magnitudes smaller than the radius of the micron particles (10^{-7}–10^{-4} m), suggesting that the contact resistance can be neglected for typical electronics applications [37].

4. Numerical simulation for determination of a universal interaction coefficient

In this study, a numerical simulation was additionally performed to determine the interaction coefficient C_1 in Eq. (9) by providing an ideal reference system. A three-dimensional Lattice Boltzmann Method (3D-LBM) was used to calculate the effective thermal conductivity of this system. The calculation was made on a cubic grid system ($100 \times 100 \times 100$) employing a D3Q15 lattice scheme [10].

For the validation of the homemade LBM code, we first considered two ideal systems (series and parallel systems), the analytic solutions of which are well known. When v_f varies from 0.1 to 0.9 at $\alpha = 100$, the mean calculation errors for the two systems are as small as 2.37% and 0.7%, respectively (see Fig. S1 in Supplementary material). We also considered another reference system where a spherical particle of radius r_p was positioned in the center of a cubic domain. The cubic domain was digitized with a grid of $100 \times 100 \times 100$, and a periodic boundary condition was given to the four lateral surfaces of the cubic domain. Hence, the cubic domain may be extended (as a building block) to a large scale at which spherical particles are uniformly distributed in a continuous matrix without overlapping. The temperatures at the top and the bottom surfaces of the cubic domain were fixed, maintaining a constant temperature difference of $\Delta T = 25$ K. The radius of the sphere was adjusted relative to the size of the cubic domain so as to reflect the volume fraction of the particle.

When increasing v_f from 0.1 to 0.45, the LBM simulation results are presented with two solid symbols in Fig. 2, corresponding to the cases of $\alpha = 100$ and 1000. Then, the present model of Eq. (9) was applied for these two sets of data, yielding $C_1 = 1.12$ for the best fit. Since particles are spherical in this case, the shape factor C_2 is simply 2. In Fig. 2, the predicted results by the present model are clearly in better agreement with the LBM results compared with the Maxwell–Eucken model predictions, denoting mean errors of 2.93% and 4.10% at $\alpha = 100$ and 1000, respectively. In the figure, the mean errors of the Maxwell–Eucken model were 8.88% and 11.12%. It is interesting to see that their prediction error grew with increasing v_f. This might be attributed to the fact that their model does not reflect the effect of inter-particle interactions that will be strengthened at higher v_f. It is also worth noting that the mean errors of the present model are much lower than the 16.96% and 20.41% of the Cheng–Vachon model, the 27.45% and 27.04% of the Lewis–Nielsen's model, and the 15.15% and 16.40% of Bruggeman's asymmetric model.

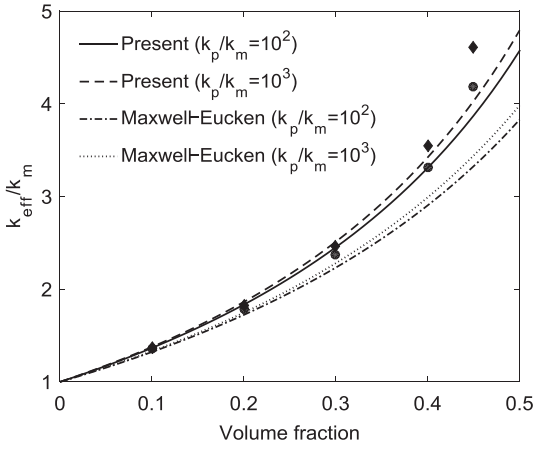

Fig. 2. Comparison of the present model predictions with numerical results from 3D-LBM at two thermal conductivity ratios. Numerical results are marked with circles (●) in the case of $\alpha = 100$, and diamonds (◆) in the case of $\alpha = 1000$. For reference, prediction results by Maxwell–Eucken model are shown with a dot-dash line and a dotted line for the two cases.

It was shown that the error of each model increased with the rise of v_f. In particular, the errors at $v_f = 0.45$ between the results of 3D-LBM and conventional models were 15–81% at $\alpha = 100$ and 14–80% at $\alpha = 1000$. With the present model, the error was reduced to 7.40% and 12.58%, respectively, showing the lowest value, but this model tends to slightly under-predict the effective thermal conductivity, so it should be used with care at $v_f \geq 0.4$.

In addition, this might raise a validity issue related to the constant treatment of C_1 particularly at high volume fractions, because the inter-particle interaction is likely strengthened with increasing v_f. However, note that the value of C_1 was resulted from the LBM simulation dataset in a range of $0 < v_f \leq 0.4$. This means that the result of $C_1 = 1.12$ might be regarded as an average impact of the interaction over the entire range of v_f. Particularly at high volume fractions where particles are frequently aggregated, the constant treatment of C_1 might not be appropriate. But, we speculated that this aggregation that maximizes the inter-particle interaction was additionally treated by another factor of C_2. Eq. (9) shows that C_2 appears as a product of C_1 in the numerator of Eq. (9), which suggests that the C_2 plays an action of supplementing the C_1 when particle aggregation occurs.

Let us describe further about physical significance of the obtained interaction coefficient ($C_1 = 1.12$). Jeffrey [38] studied the interaction between pairs of spherical particles that are randomly distributed in a matrix, and derived the following analytic model.

$$\frac{k_{eff}}{k_m} = 1 + 3\beta v_f + F(\beta) v_f^2 + O\left(v_f^3\right) \tag{11}$$

Here, β is calculated by $(k_p\text{-}k_m)/(k_p + 2k_m)$. The coefficient $F(\beta)$ of the quadratic term of v_f is zero at $\alpha = 1$ and becomes close to 4.51 after a monotonic increase when α increases up to 1000. To compare with Eq. (11), Eq. (9) may be expressed as a series function when $C_1 v_f < 1$, as seen in Eq. (12).

$$\frac{k_{eff}}{k_m} = 1 + (1 + C_2) C_1 \beta v_f + (1 + C_2)\left(C_1 \beta v_f\right)^2 + (1 + C_2)\left(C_1 \beta v_f\right)^3 + \cdots \tag{12}$$

One may notice a remarkable similarity between Eqs. (11) and (12). Substituting the aforementioned results ($C_1 = 1.12$; $C_2 = 2$ for spherical particles; $\beta \cong 1$ at $\alpha = 1000$) into Eq. (12), the coefficients of v_f and v_f^2 in Eq. (12) become 3.36 and 3.76, which are in reasonable agreement with 3 and 4.51 in Eq. (11), respectively. Taking these promising results into account, we believe that our model enables a reasonable prediction of k_{eff} even with the practical approximation of $C_1 = 1.12$.

5. Validation of the model prediction with empirically-driven shape coefficients

Fig. 3 shows the comparison of our model prediction to Carson's experimental results [39]. Carson [39] measured effective thermal conductivities of guar gum matrices (carbohydrate polymer gel, $k_m = 0.6$ W/m K) mixed with aluminum particles ($k_p = 209$ W/m K) in a range of $v_f = 0$–0.6. Since the aluminum particles had an aspect ratio of unity with 5 mm diameter and 5 mm height, the particles were approximated to be spherical, yielding $C_2 = 2$ in accordance with Eq. (10). Given a constant interaction coefficient ($C_1 = 1.12$), we estimated effective thermal conductivities for $\alpha = 348$ until $v_f \leq 0.5$. As shown in Fig. 3, our model predictions are in good agreement with their experimental data, in which the mean prediction error is as small as ~6%. It might be concluded that $C_1 = 1.12$ is a reasonable approximation unless the particles get clo-

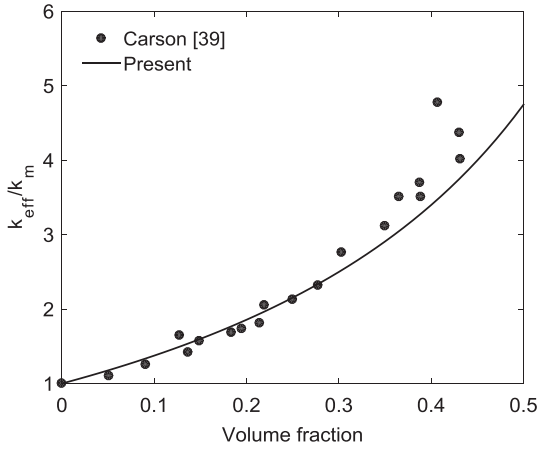

Fig. 3. Comparison of experimental data [38] and the model prediction in which spherical particles were randomly distributed in a matrix without aggregation (k_m = 0.6 W/m K, k_p = 209 W/m K, C_1 = 1.12, C_2 = 2). Experimental data are marked with solid circles (●).

ser too much at very high volume fractions. In the rest of this work, C_1 = 1.12 was used consistently.

It is well known that particle aggregation can significantly influence the effective thermal conductivity of a particle-reinforced matrix [8,24,40]. In our model, the aggregation effect is implemented through the shape coefficient (C_2), which is a function of an aspect ratio of aggregates. However, it is not straightforward to obtain aspect ratios of aggregates theoretically, because aggregation is a complicated process depending on multiple experimental parameters such as volume fraction of particles and sample fabrication parameters. Thus, we extracted an average aspect ratio

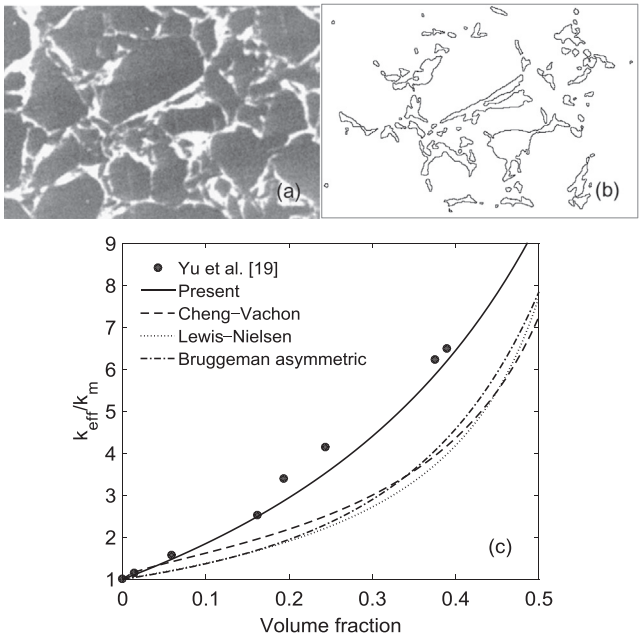

Fig. 4. Experimental data [19] and model predictions with SEM image analysis. Shape coefficient (C_2 = 5.79) was obtained from the image analysis of the sample. (a) SEM image of the sample (PS + AlN, v_f = 0.25) where dark grains are PS matrix and white streaks denote aggregated particles of AlN, (b) Identified particle aggregates each enclosed with a line following image analysis, (c) Comparisons of the experimental data and the model predictions (k_m = 0.15 W/m K, k_p = 160 W/m K). Experimental data were marked with solid circles (●). (Reprinted from Composites: Part A, 33, Yu et al., Thermal conductivity of polystyrene-aluminum nitride composite, 289–292, Copyright (2002), with permission from Elsevier).

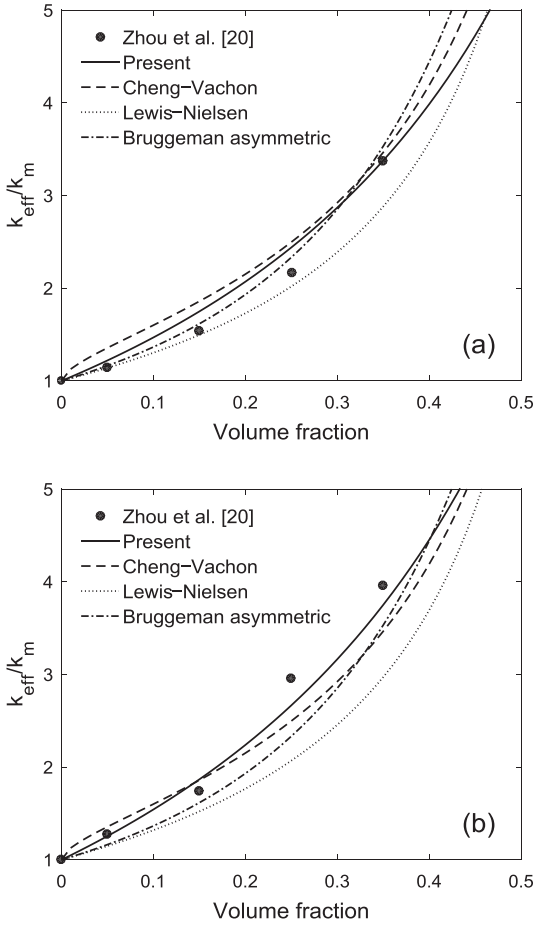

Fig. 5. Experimental data [20] and model predictions (k_m = 0.26 W/m K, k_p = 65 W/m K). Experimental data were marked with solid circles (●). Shape coefficients were obtained from the image analysis for the sample (HDPE + BN, v_f = 0.35). (a) Melted mix (C_2 = 2.77), (b) Powder mix (C_2 = 3.38).

of aggregates from scanning electron microscope (SEM) images available from literature [19,20] and used the resulting value of C_2 for predicting effective thermal conductivities, and then compared this with the experimental data.

Yu et al. [19] measured effective thermal conductivities of a polystyrene matrix (k_m = 0.15 W/m K) with aluminum nitride particles (k_p = 160 W/m K) by changing the volume fraction of particles. Fig. 4(a) shows the SEM image of the sample prepared at v_f = 0.25. The large dark grains are the matrix particles, whereas the white streaks surrounding the matrix particles denote aggregated particles. Using ImageJ ver. 1.51j8, the SEM image was analyzed to extract shape information from the aggregates. By adjusting the image contrast, we could identify each of the white streaks, as presented in Fig. 4(b). Treating any enclosed area as a single aggregate, we obtained the corresponding cross-section area (S) and maximum length (l_{max}) per aggregate. Aggregates (white spots) that are connected to the boundaries of the image were excluded from the analysis. Those irregular-shaped aggregates were then approximated to ellipsoids with different aspect ratios. By applying Eqs. (13a) and (13b), an aspect ratio of each aggregate ($r_{a,i}$) and an area-weighted average aspect ratio (r_a) could respectively be obtained and then plugged in Eq. (10) to calculate a shape coefficient (C_2). As a result, the average shape coefficient for Fig. 4 (a) was calculated to be $C_2 \sim 5.79$ with an average aspect ratio (r_a) of 4.63.

$$r_{a,i} = \frac{4S_i}{\pi l_{max,i}^2} \tag{13a}$$

Table 3
Comparison between experimental data and prediction results from the previous models and our model. Experimental data were taken from the literature in which Zhou et al. [20] prepared the composite sample by two different methods according to the treatment of the matrix: 'melted mix' and 'powder mix.' The predictions of Lewis–Nielsen and our models were implemented with the shape coefficients determined from SEM image analysis.

	Yu et al. [19]		Zhou et al. [20] Melted mix		Zhou et al. [20] Powder mix	
	Average error (E)	Error at $v_f = 0.25$	Average error (E)	Error at $v_f = 0.35$	Average error (E)	Error at $v_f = 0.35$
Our model	6%	15%	6%	0.1%	4%	5%
Cheng–Vachon	22%	39%	11%	2%	8%	12%
Lewis–Nielsen	29% ($r_a = 4.63$)	46% ($r_a = 4.63$)	5% ($r_a = 2.27$)	14% ($r_a = 2.27$)	15% ($r_a = 2.85$)	25% ($r_a = 2.85$)
Bruggeman asymmetric	27%	44%	3%	4%	9%	10%

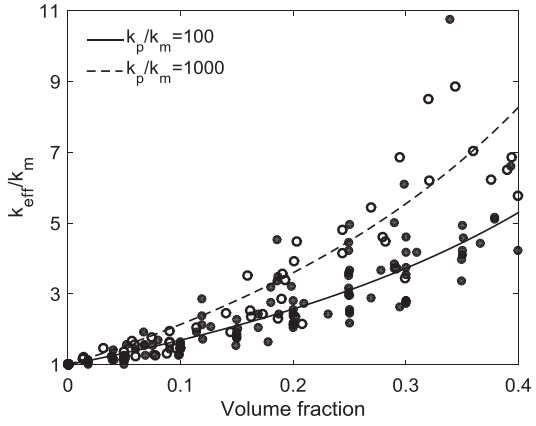

Fig. 6. Scatter plot of experimental data ($\alpha \geq 100$) against particles' volume fraction, where open circles are experimental data with $\alpha \geq 1000$, and filled circles are experimental data with $100 \leq \alpha \leq 1000$. The solid and dashed lines represent the predictions using the present model as a guidance.

$$r_a = \sum_{i=1} S_i r_{a,i} \Big/ \sum_{i=1} S_i \tag{13b}$$

where i is an index of aggregates in the SEM images.

Applying $C_1 = 1.12$ and $C_2 = 5.79$ (at $r_a = 4.63$) to Eq. (9), effective thermal conductivities were calculated at various volume fractions ranging from 0 to 0.5. Fig. 4(c) proves that our model predictions are in much better agreement with the experimental data than the previous models. Note that the mean error of our model is only ~6% in the entire range of volume fractions, while the other models show more than 40% error. In particular, the superiority of our model may be highlighted when compared with the Lewis–Nielsen model in which the same shape coefficient was used.

Likewise, this model validation process was repeated for Zhou et al.'s experimental data [20] in order to expand the validity of our model prediction. Their composite sample was made of boron nitride particles ($k_p = 65$ W/m K) in a high density polyethylene matrix ($k_m = 0.26$ W/m K). Zhou et al. [20] attempted to change the internal structures of the sample by mixing the particles with matrix powder that had melted or was still in solid phase. They provided two SEM images for the samples prepared by two different mixing methods (referred to as 'melted mix' and 'powder mix') at $v_f = 0.35$. The aforementioned image analysis was performed to obtain a shape coefficient for each sample.

Fig. 5(a) and (b) show the comparison of our model prediction with $C_2 = 2.77$ ($r_a = 2.27$) and $C_2 = 3.38$ ($r_a = 2.85$) to the experimental data for the samples prepared by the 'melted mix' and by the 'powder mix,' respectively. Note that the two shape coefficients resulted from the image analysis for the two cases. We also compared our prediction models with the previous models. The prediction errors of the whole models are summarized in Table 3. Overall, all the models showed good prediction with an average error

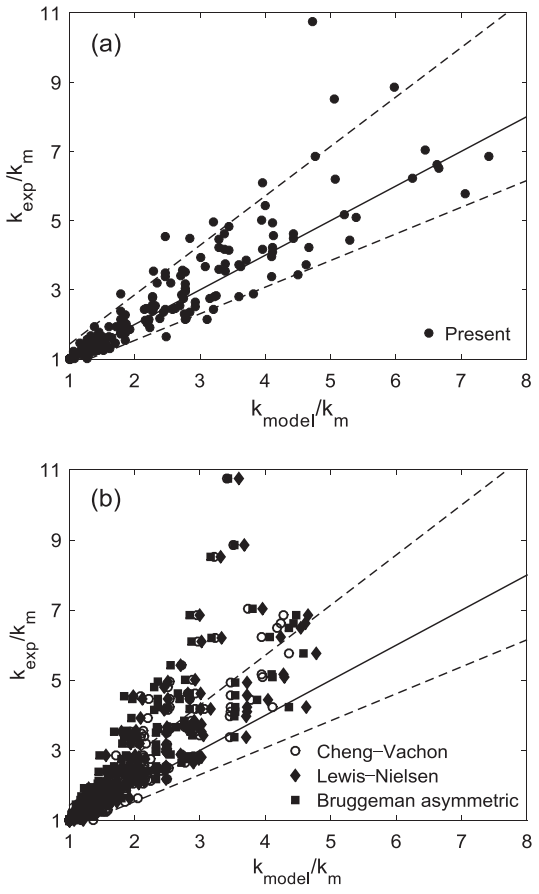

Fig. 7. Comparison between all experimental data (k_{exp}) and (previous & present) model predictions (k_{model}); (a) Present model vs experiments, (b) previous models vs experiments. Solid line represents the perfect prediction as a reference where model predictions coincide with experimental data. Dashed line represents the border where the prediction error between model predictions and experimental data is ±30%.

below 15%, unlike the case of Yu et al.'s sample [19]. This may result from a smaller aspect ratio of aggregates (lowering C_2) as well as a lower thermal conductivity of particles (lowering α) in Zhou et al.'s samples [20], both of which reduce the relative contribution of aggregation to an effective thermal conductivity. It should be recalled that in Table 1, the three previous models considered in Fig. 5 worked well when $\alpha < 1000$, and Zhou et al.'s sample [20] has a low α (= 250) relative to Yu et al.'s sample ($\alpha = 1066$) [19].

Another thing to note is that our model yielded the best predictions at $v_f = 0.35$ where the shape coefficients were obtained directly from the SEM images, in contrast to the Lewis–Nielsen model presenting the worst prediction accuracy with the same

shape coefficient. All of these findings emphasize the significance of considering aggregate microstructures in the prediction of effective thermal conductivity, and highlight that our model is the most promising as long as the internal structures of samples are available. The question of what will happen if the internal structure of a target sample is unknown may be raised here. This is an important issue for practicality because a priori prediction of effective thermal conductivity is sometimes required in a preliminary design stage.

To facilitate the utility of our model, we attempted to derive an empirical correlation between key experimental parameters (volume fraction, v_f, and thermal conductivity ratio, α) and aspect ratio. We collected as much experimental data as we were aware of from literature, and used them for the derivation of correlation when $0 \le v_f \le 0.4$ and $\alpha \ge 100$ [16–26,28]. In Fig. 6, the experimental datasets were divided into two groups of $100 \le \alpha < 1000$ and $\alpha \ge 1000$ simply for convenience, and presented with solid circles and open circles, respectively. At first, each dataset was best fitted based on our model by tuning an aspect ratio at each volume fraction under the approximation of $\alpha = 100$ or 1000, and the resulting fitted curve for each group was also presented with solid or dotted lines in Fig. 6, respectively. Although the experimental data were scattered considerably, the two curves seemingly represent the trends of the experimental data quite well. The fitting process was then expanded for the whole experimental data without the approximation of α, which finally provides an empirical equation to express an apparent aspect ratio as a function of the two independent parameters (v_f and α) as:

$$r_a = 1 + 0.48(\log\alpha)^{2.17} v_f^{0.30} \tag{14}$$

Eq. (14) was utilized to estimate a shape coefficient (C_2) corresponding to each data point in Fig. 6. Based on the set of C_2 and $C_1 = 1.12$, the values of k_{eff}/k_m were calculated by our model and compared with the corresponding values from the experiments in Fig. 7(a). The scatter plot in Fig. 7(a) displays how much the model predictions deviated from the experimental measurements. In the figure, a solid line having a slope of unity denotes the perfect prediction as a reference line, whereas the two dashed lines represent an error range of ±30%. Note that most of the predicted data safely fall between the dashed lines, revealing an average error of ~11% as a whole. In contrast, the other models show a strong tendency of underestimation when effective thermal conductivity increases beyond $k_{eff}/k_m \sim 2$. This strongly supports our model being the most promising for a priori prediction of an effective thermal conductivity with lack of structural information of aggregates, and can be widely utilized in a variety of experimental conditions where other models are not applicable.

6. Conclusion

In this study, a new analytical model was developed to establish a practical and more reliable means of prediction of an effective thermal conductivity of a particle-reinforced composite material, particularly in electronics applications where high-conductivity particles are normally added in a polymer matrix. Comprehensive evaluation of the existing models was performed with increasing particle conductivity, and this resulted in an interesting asymptotic behavior of the previous models at the extreme condition. Based on Maxwell's approximation scheme, a new analytical model was derived not only to incorporate the primary factors and most of the secondary factors affecting the heat conduction with simplification, but also to be consistent with the asymptotic functional forms at the limiting condition. An interaction coefficient (C_1) was introduced for reflecting the inter-particle interaction among the secondary factors and was determined to be 1.12 through 3D-LBM simulations, revealing that the value of C_1 is practically quasi-universal. Moreover, a shape coefficient (C_2) characterizing the particle shape and aggregation was obtained through image analysis for SEM images of samples. With these key coefficients, the present model was systematically validated with a multitude of experimental data from literature, highlighting its high prediction accuracy and applicability to extreme conditions (e.g., with very high-conductivity particles at high volume fractions) where other existing models are not suitable for use. For further facilitating the utility of the present model, an empirical correlation between experimental parameters and a shape coefficient was derived taking into consideration a large number of existing experimental data from literature. We demonstrated that this elaborated correlation is powerful, enabling a priori prediction of effective thermal conductivity within ±30% prediction error even in electronics application.

Conflict of interest

The authors declared that there is no conflict of interest.

Acknowledgement

This work was supported by a two-year research grant from Pusan National University.

Appendix A. Summary of representative previous analytical models

Model names/grouping	Formulations	Comments
Parallel model [41]/Group A	$k_{eff} = v_f k_p + (1 - v_f) k_m$	Vertically laminated structure
Series model [41]/Group A	$k_{eff}^{-1} = v_f k_p^{-1} + (1 - v_f) k_m^{-1}$	Horizontally laminated structure
Geometric mean model [41]/Group A	$k_{eff} = k_p^{v_f} k_m^{1-v_f}$	Internal conductive networks (percolation)
Maxwell–Eucken model [32,41]/Group A	$k_{eff} = k_m \frac{1+2\beta v_f}{1-\beta v_f}$ where $\beta = \frac{k_p - k_m}{k_p + 2k_m}$	Well-separated spheres without interaction
Bruggeman symmetric model [5]/Group A	$\frac{k_p - k_{eff}}{k_p + 2k_{eff}} + \frac{k_m - k_{eff}}{k_m + 2k_{eff}} = 0$	Significant increase for $v_f > 1/3$, high α and isotropic spherical particles
Cheng–Vachon model [42]/Group B	when $k_p > k_m$, $\frac{1}{k_{eff}} = \frac{1}{\sqrt{C(k_m - k_p)[k_m + B(k_p - k_m)]}} \ln \frac{\sqrt{k_m + B(k_p - k_m)} + \frac{B}{2}\sqrt{C(k_m - k_p)}}{\sqrt{k_m + B(k_p - k_m)} - \frac{B}{2}\sqrt{C(k_m - k_p)}} + \frac{1-B}{k_m}$ where $B = \sqrt{3v_f/2}, C = -4\sqrt{2/(3v_f)}$	Parabolic (2nd-order polynomial) distribution of particles in space

Appendix A (*continued*)

Model names/grouping	Formulations	Comments
Lewis–Nielsen model [43]/ Group C	$k_{eff} = k_m \frac{1+A\beta v_f}{1-\psi\beta v_f}$ where $\beta = \frac{k_p - k_m}{k_p + Ak_m}, \psi = 1 + \left(\frac{1-v_{f,max}}{v_{f,max}^2}\right) v_f, A = k_E - 1$	Analogy from elastic moduli$A$: shape parameter k_E: Einstein coefficient $v_{f,max}$: packing fraction
Zhou model [44]/Group D	$k_{eff} = \frac{k_p k_m}{v_d k_m + (1-v_d)k_p} \frac{v_f}{v_d} (\overline{\cos\theta})^2 + \left[\overline{\cos\theta} - \frac{v_f}{v_d}(\overline{\cos\theta})^2\right] k_m$ for simple and cubic lattice structure $\left(\theta = 0, v_d = v_f^{1/3}\right)$	Heat-transfer passages and orientation in continuous matrix Θ: angle between the axis of heat-transfer passages and the direction defined by the thermal flow v_d: volume fraction of fillers in a heat-transfer passage ($v_d \neq v_f$)
Bruggeman asymmetric model [5]/Group A	$1 - v_f = \frac{k_p - k_{eff}}{k_p - k_m} \left(\frac{k_m}{k_{eff}}\right)^{1/3}$	Spherical particles, continuous matrix, and particle interaction
Russell model [45]/Group A	$k_{eff} = k_m \left[\frac{v_f^{2/3} + \frac{k_m}{k_p}\left(1 - v_f^{2/3}\right)}{v_f^{2/3} - v_f + \frac{k_m}{k_p}\left(v_f + 1 - v_f^{2/3}\right)}\right]$	Cube-shaped particles with the same size
Co-continuous model [46]/ Group A	$k_{eff} = \frac{K_s}{2}\left[\sqrt{1 + \frac{8K_p}{K_s}} - 1\right]$ where $K_P = v_f k_p + (1 - v_f)k_m, K_s^{-1} = v_f k_p^{-1} + (1 - v_f)k_m^{-1}$	Isotropic material where all phases are continuous

Appendix B. Supplementary material

Supplementary data associated with this article can be found, in the online version, at https://doi.org/10.1016/j.ijheatmasstransfer.2018.11.107.

References

[1] X. Chen, Y. Su, D. Reay, S. Riffat, Recent research developments in polymer heat exchangers – a review, Renew. Sustain. Energy Rev. 60 (2016) 1367–1386.
[2] A.R.J. Hussain, A.A. Alahyari, S.A. Eastman, C. Thibaud-Erkey, S. Johnston, M.J. Sobkowicz, Review of polymers for heat exchanger applications: factors concerning thermal conductivity, Appl. Therm. Eng. 113 (2017) 1118–1127.
[3] D.J. Kim, M.J. Jo, S.Y. Nam, A review of polymer–nanocomposite electrolyte membranes for fuel cell application, J. Ind. Eng. Chem. 21 (2015) 36–52.
[4] X. Lu, G. Xu, Thermally conductive polymer composites for electronic packaging, J. Appl. Polym. Sci. 65 (13) (1997) 2733–2738.
[5] R. Prasher, Thermal interface materials: historical perspective, status, and future directions, Proc. IEEE 94 (8) (2006) 1571–1586.
[6] A.L. Moore, L. Shi, Emerging challenges and materials for thermal management of electronics, Mater. Today 17 (4) (2014) 163–174.
[7] X. Huang, P. Jiang, T. Tanaka, A review of dielectric polymer composites with high thermal conductivity, IEEE Electr. Insul. Mag. 27 (4) (2011) 8–16.
[8] B. Chen, H. Chen, V.V. Ginzburg, Y. Yang, J. Yang, W. Liu, Y. Huang, L. Du, Thermal conductivity of polymer-based composites: Fundamentals and applications, Prog. Polym. Sci. 59 (2016) 41–85.
[9] Y. Xu, K. Yagi, Automatic FEM model generation for evaluating thermal conductivity of composite with random materials arrangement, Comput. Mater. Sci. 30 (3) (2004) 242–250.
[10] M. Wang, N. Pan, Predictions of effective physical properties of complex multiphase materials, Mater. Sci. Eng. R 63 (1) (2008) 1–30.
[11] M. Aadmi, M. Karkri, L. Ibos, M.E. Hammouti, Effective thermal conductivity of random two-phase composites, J. Reinf. Plast. Compos. 33 (1) (2014) 69–80.
[12] T. Oppelt, T. Urbaneck, H. Böhme, B. Platzer, Numerical investigation of effective thermal conductivity for two-phase composites using a discrete model, Appl. Therm. Eng. 115 (2017) 1–8.
[13] S.V. Syrodoy, G.V. Kuznetsov, N.Y. Gutareva, V.V. Salomatov, The efficiency of heat transfer through the ash deposits on the heat exchange surfaces by burning coal and coal-water fuels, J. Energy Inst. 91 (2018) 1091–1101.
[14] L. Loh, C. Chua, W. Yeong, J. Song, M. Mapar, S. Sing, Z. Liu, D. Zhang, Numerical investigation and an effective modelling on the Selective Laser Melting (SLM) process with aluminium alloy 6061, Int. J. Heat Mass Transf. 80 (2015) 288–300.
[15] P. Peyre, Y. Rouchausse, D. Defauchy, G. Régnier, Experimental and numerical analysis of the selective laser sintering (SLS) of PA12 and PEKK semi-crystalline polymers, J. Mater. Process. Technol. 225 (2015) 326–336.
[16] C.P. Wong, R.S. Bollampally, Thermal conductivity, elastic modulus, and coefficient of thermal expansion of polymer composites filled with ceramic particles for electronic packaging, J. Appl. Polym. Sci. 74 (14) (1999) 3396–3403.
[17] D.W. Sundstrom, Y. Lee, Thermal conductivity of polymers filled with particulate solids, J. Appl. Polym. Sci. 16 (12) (1972) 3159–3167.
[18] H. Tu, L. Ye, Thermal conductive PS/graphite composites, Polym. Adv. Technol. 20 (1) (2009) 21–27.
[19] S. Yu, P. Hing, X. Hu, Thermal conductivity of polystyrene–aluminum nitride composite, Compos. A Appl. Sci. Manuf. 33 (2) (2002) 289–292.
[20] W. Zhou, S. Qi, Q. An, H. Zhao, N. Liu, Thermal conductivity of boron nitride reinforced polyethylene composites, Mater. Res. Bull. 42 (10) (2007) 1863–1873.
[21] A. Boudenne, L. Ibos, M. Fois, J.C. Majesté, E. Géhin, Electrical and thermal behavior of polypropylene filled with copper particles, Compos. A Appl. Sci. Manuf. 36 (11) (2005) 1545–1554.
[22] I. Krupa, I. Chodák, Physical properties of thermoplastic/graphite composites, Eur. Polym. J. 37 (11) (2001) 2159–2168.
[23] Y. Agari, A. Ueda, M. Tanaka, S. Nagai, Thermal conductivity of a polymer filled with particles in the wide range from low to super-high volume content, J. Appl. Polym. Sci. 40 (5) (1990) 929–941.
[24] Y. Agari, A. Ueda, S. Nagai, Thermal conductivities of composites in several types of dispersion systems, J. Appl. Polym. Sci. 42 (6) (1991) 1665–1669.
[25] P. Bujard, J.P. Ansermet, Thermally conductive aluminium nitride-filled epoxy resin (for electronic packaging), in: Fifth Annual IEEE Semiconductor Thermal and Temperature Measurement Symposium, 1989, pp. 126–130.
[26] I. Krupa, I. Novák, I. Chodák, Electrically and thermally conductive polyethylene/graphite composites and their mechanical properties, Synth. Met. 145 (2) (2004) 245–252.
[27] D.M. Liu, W.H. Tuan, Microstructure and thermal conduction properties of Al2O3-Ag composites, Acta Materialia 44 (2) (1996) 813–818.
[28] A. Boudenne, L. Ibos, M. Fois, E. Gehin, J. Majeste, Thermophysical properties of polypropylene/aluminum composites, J. Polym. Sci., Part B: Polym. Phys. 42 (4) (2004) 722–732.
[29] S.C. Cheng, R.I. Vachon, A technique for predicting the thermal conductivity of suspensions, emulsions and porous materials, Int. J. Heat Mass Transf. 13 (3) (1970) 537–546.
[30] J.K. Carson, J. Wang, M.F. North, D.J. Cleland, Effective thermal conductivity prediction of foods using composition and temperature data, J. Food Eng. 175 (2016) 65–73.
[31] S. Torquato, Random Heterogeneous Materials, first ed., Springer, New York, 2002, pp. 460–488.
[32] J.K. Carson, S.J. Lovatt, D.J. Tanner, A.C. Cleland, Thermal conductivity bounds for isotropic, porous materials, Int. J. Heat Mass Transf. 48 (11) (2005) 2150–2158.
[33] J.C. Maxwell, A Treatise on Electricity and Magnetism, first ed., Clarendon Press, Oxford, 1873.
[34] H. Hatta, M. Taya, Effective thermal conductivity of a misoriented short fiber composite, J. Appl. Phys. 58 (1985) 2478–2486.
[35] A.G. Every, Y. Tzou, D.P.H. Hasselman, R. Raj, The effect of particle size on the thermal conductivity of ZnS/diamond composites, Acta Metallurgica Et Materialia 40 (1) (1992) 123–129.
[36] P.E. Hopkins, L.M. Phinney, J.R. Serrano, T.E. Beechem, Effects of surface roughness and oxide layer on the thermal boundary conductance at aluminum/silicon interfaces, Phys. Rev. B 82 (8) (2010).

[37] W. Evans, R. Prasher, J. Fish, P. Meakin, P. Phelan, P. Keblinski, Effect of aggregation and interfacial thermal resistance on thermal conductivity of nanocomposites and colloidal nanofluids, Int. J. Heat Mass Transf. 51 (5) (2008) 1431–1438.
[38] D.J. Jeffrey, Conduction through a random suspension of spheres, Proc. Roy. Soc. A 335 (1602) (1973) 355–367.
[39] J.K. Carson, Measurement and modelling of the thermal conductivity of dispersed aluminium composites, Int. Commun. Heat Mass Transfer 38 (8) (2011) 1024–1028.
[40] I.A. Tsekmes, R. Kochetov, P.H.F. Morshuis, J.J. Smit, Thermal conductivity of polymeric composites: a review, in: 2013 IEEE International Conference on Solid Dielectrics, 2013, pp. 678–681.
[41] D.S. McLachlan, M. Blaszkiewicz, R.E. Newnham, Electrical resistivity of composites, J. Am. Ceram. Soc. 73 (8) (1990) 2187–2203.
[42] S.C. Cheng, R.I. Vachon, The prediction of the thermal conductivity of two and three phase solid heterogeneous mixtures, Int. J. Heat Mass Transf. 12 (3) (1969) 249–264.
[43] L.E. Nielsen, The thermal and electrical conductivity of two-phase systems, Ind. Eng. Chem. Fundam. 13 (1) (1974) 17–20.
[44] H. Zhou, S. Zhang, M. Yang, The effect of heat-transfer passages on the effective thermal conductivity of high filler loading composite materials, Compos. Sci. Technol. 67 (6) (2007) 1035–1040.
[45] H.W. Russell, Principles of heat flow in porous insulators, J. Am. Ceram. Soc. 18 (1935) 1–5.
[46] J. Wang, J.K. Carson, M.F. North, D.J. Cleland, A new structural model of effective thermal conductivity for heterogeneous materials with co-continuous phases, Int. J. Heat Mass Transf. 51 (9) (2008) 2389–2397.